Published in final edited form as:
Nat Mater. 2018 September ; 17(9): 827–833. doi:10.1038/s41563-018-0133-2.

Surface Distortion as a Unifying Concept and Descriptor in Oxygen Reduction Reaction Electrocatalysis

Raphaël Chattot[1,2,*], **Olivier Le Bacq**[3], **Vera Beermann**[4], **Stefanie Kühl**[4], **Juan Herranz**[5], **Sebastian Henning**[5], **Laura Kühn**[6], **Tristan Asset**[1], **Laure Guétaz**[7], **Gilles Renou**[3], **Jakub Drnec**[2], **Pierre Bordet**[8], **Alain Pasturel**[3], **Alexander Eychmüller**[6], **Thomas J. Schmidt**[5,9], **Peter Strasser**[4], **Laetitia Dubau**[1], and **Frédéric Maillard**[1,*]

[1]Univ. Grenoble Alpes, CNRS, Grenoble INP ⊥, Univ. Savoie Mont Blanc, LEPMI, 38000 Grenoble, France [2]ESRF-The European Synchrotron, ID 31 Beamline, 38043 Grenoble, France [3]Univ. Grenoble Alpes, CNRS, Grenoble INP ⊥, SIMAP, 38000 Grenoble, France [4]Electrochemical Energy, Catalysis and Material Science Laboratory, Department of Chemistry, Technische Universität Berlin, 10623 Berlin, Germany [5]Electrochemistry Laboratory, Paul Scherrer Institut, 5232 Villigen, Switzerland [6]Physical Chemistry, Technische Universität Dresden, 01062 Dresden, Germany [7]CEA, LITEN, LCPEM, 38054 Grenoble, France [8]CNRS, Institut Néel, F-38000 Grenoble, France [9]Laboratory of Physical Chemistry, ETH Zurich, 8093 Zurich, Switzerland

Abstract

Tuning the surface structure at the atomic level is of primary importance to simultaneously meet the electrocatalytic performance and stability criteria required for the development of low-temperature proton-exchange membrane fuel cells (PEMFCs). However, transposing the knowledge acquired on extended, model surfaces to practical nanomaterials remains highly challenging. Here, we propose the 'Surface Distortion' as a novel structural descriptor, which is able to reconciliate and unify seemingly opposing notions and contradictory experimental observations in regards to the electrocatalytic oxygen reduction reaction (ORR) reactivity. Beyond its unifying character, we show that surface distortion is pivotal to rationalize the electrocatalytic properties of state-of-art of PtNi/C nanocatalysts with distinct atomic composition, size, shape and degree of surface defectiveness under simulated PEMFC cathode environment. Our study brings

*(RC) raphael.chattot@grenoble-inp.org; (FM) frederic.maillard@lepmi.grenoble-inp.fr.
⊥Institute of Engineering Univ. Grenoble Alpes

Data Availability. The datasets generated during and/or analysed during the current study are available from the corresponding author on reasonable request.

Author contributions

R.C., L.D. and F.M. conceived the experiments. R.C. carried out the experiments, analysed the data and wrote the first version of the manuscript. V.B., S.K. and L.K. contributed to material synthesis. J.H., S.H. and T.A. contributed to electrochemical measurements. L.G. and G.R. contributed to HRTEM and STEM/X-EDS experiments. J.D. performed the WAXS experiments and P.B. the Rietveld analysis. O.L.B. and A.P. carried out the DFT calculations. All authors contributed to the discussion section and the finalization of the text and Figures of the manuscript.

Europe PMC Funders Author Manuscripts

fundamental and practical insights into the role of surface defects in electrocatalysis and highlights strategies to design more durable ORR nanocatalysts.

In the current climatic and energetic context, where energy production and transportation sectors need breakthroughs to decrease anthropogenic carbon dioxide emissions, electrochemical conversion and storage devices such as proton-exchange membrane fuel cells (PEMFCs), and water electrolysers (PEMWEs) represent appealing solutions 1–3. However, the widespread commercialization of PEMFC systems remains limited by the high platinum (Pt) content needed to compensate for the sluggish oxygen reduction reaction (ORR) kinetics occurring at the device's cathode 4,5. An extended $Pt_3Ni(111)$-skin single crystal has been experimentally reported as the most active surface for the ORR 6, due to its near-optimal position of the Pt valence *d*-band centre 7 resulting from synergetic contributions of strain 8–12, ligand 13,14 and ensemble 15,16 effects. Transposing the high ORR activity of this extended (and model) surface to real-life nanocatalysts presupposes that its ideal atomic arrangement can be reproduced at the nanoscale. In practice, thought, preferentially-shaped bimetallic octahedral nanoparticles (owing to their exclusive (111)-oriented facets) show high initial ORR activity but suffer from prejudicial stability issues under simulated PEMFC cathode operating conditions (high temperature, low pH, oxidizing atmosphere and electrochemical potential) 17. Maintaining the octahedral shape (*i.e.* a high concentration of highly-coordinated surface atoms) and minimizing the amount of dissolved Ni atoms (especially from the surface and near-surface layers) are pivotal to the success of 'surface science-inspired' nanocatalysts 17–19. Alternatively, as predicted by density functional theory (DFT) calculations 20–25 and experimentally verified 26–28, another approach towards high catalytic ORR rates consists of generating active locally-concave Pt surface sites. In this approach, each coordinatively-distinct catalytic site features a unique reactivity due to its unique local structural environment 29, the latter being possibly modified by the presence of point and surface defects. Here, the atomic arrangement is essential as well, but strikingly, structural disorder is beneficial, not detrimental to the ORR kinetics. These seemingly opposed approaches (keeping structural order *vs.* introducing structural disorder) have raised confusion and heated debates in the scientific community. The debates are further fuelled by the lack of experimental techniques, which are available to measure and quantify structural and chemical order/disorder in the topmost surface and the near-surface layers, thereby preventing the identification of unambiguous structure-activity relationships for bimetallic nanocatalysts.

In this contribution, the two seemingly opposite strategies toward highly active ORR catalytic sites described above are reconciled by introducing Surface Distortion, a structural descriptor derived from Rietveld refinement of synchrotron wide-angle X-ray scattering (WAXS) measurements. Our proposal is based on a large series of different key PtNi catalysts, including some of today's state of art PtNi nanoalloys with highly desirable ORR activity. The results show non-trivial structural disorder-electrocatalytic activity relationships for bimetallic nanocatalysts and demonstrate, through chemical and electrochemical ageing of the PtNi materials, that surface distortion controls the ORR activity in the long-term.

Europe PMC Funders Author Manuscripts

Fig. 1.a-1.f displays transmission electron microscopy (TEM) images, correspondingly derived particle size distributions and scanning transmission electron microscopy / X-ray energy dispersive spectroscopy (STEM/X-EDS) elemental maps of spherical PtNi/C (Sphere PtNi/C), cubic PtNi/C (Cube PtNi/C), octahedral PtNi/C (Octahedron PtNi/C), hollow PtNi/C (Hollow PtNi/C), unsupported PtNi aerogel (Aerogel PtNi) and spongy (Sponge PtNi/C) PtNi catalysts evaluated in this study. Four reference materials were also used, namely a commercial Pt/C catalyst purchased from Tanaka Kikinzoku Kogyo (Pt/C TKK), cubic Pt/C (Cube Pt/C), aggregated Pt/C (A-Pt/C) and aggregated PtNi/C (A-PtNi/C) nanoparticles. Representative TEM images and associated particle size distributions for these reference materials can be found in Fig. S1 of the Supplementary Information.

As shown by Fig. 1, the 'structurally-ordered' catalysts (*i.e.* Sphere, Cube and Octahedron PtNi/C) feature *ca.* 8-10 nm isolated and monocrystalline PtNi nanoparticles of different shapes (respectively spherical, cubic and octahedral), while the 'structurally-disordered' PtNi nanoparticles are composed of *ca.* 3-5 nm aggregated crystallites interconnected by grain boundaries (*i.e.* are polycrystalline, see Hollow PtNi/C, Aerogel PtNi and Sponge PtNi/C). The differences in crystallinity and surface roughness between these two families of catalysts are highlighted by the high-angle annular dark field-high resolution STEM (HAADF-HRSTEM) images and the corresponding fast Fourier transforms shown in Fig. 1.g-1.h.

Rietveld refinement of synchrotron WAXS patterns (examples of WAXS patterns are displayed in Fig. 2.a) was performed to extract the crystal structure, crystallite size, lattice parameter and microstrain of the different PtNi catalysts. Microstrain, also referred as 'local lattice strain', is a parameter of choice to investigate a crystal 'defectiveness' as it quantifies local deviations of the atoms from their ideal positions in the crystal structure, such as those induced by structural defects (stacking faults, twins, grain boundaries, and/or dislocation arrays). As schematically shown by Fig. 2.a, microstrain, finite crystallite size and instrumental errors lead to WAXS peaks broadening but do not change the position of the X-ray reflections, the latter being related to the global Pt:Ni atomic ratio *i.e.* to 'macrostrain' (sometimes also referred to as 'strain' or 'global strain' in material science 30).

Based on these experimental data, the various sources of microstrain in bimetallic nanocatalysts are rationalized as schematically illustrated in Fig. 2.b. In the first place, slight or no microstrain is measured on pure and monocrystalline Pt/C catalysts (case (i) in Fig. 2.b, observed for Pt/C TKK and Cube Pt/C in Fig. 3.a), suggesting that structural order is possible for this type of materials. However, the introduction of grain boundaries in the nanocatalyst (*i.e.* the formation of polycrystalline nanoparticles) results in structural disorder due to local crystal cell volume expansion/contraction, 31 and higher microstrain values (case (ii) in Fig. 2.b, observed independently from other contributions only for A-Pt/C in Fig. 3.a). It is also noteworthy that the microstrain values measured for supposedly defect-free monocrystalline 'structurally-ordered' PtNi nanoparticles vary almost linearly with the Ni content (Fig. 3.a) This chemical composition-microstrain relationship was confirmed by DFT calculations (see Fig.3.b for computational details, Eqs. S1-S3 and Figs. S2-S3 in the Supplementary Information), which considered the chemical disorder induced by the locally heterogeneous distribution of Pt and Ni atoms within the nanoalloy (*i.e.* the local variations

of the crystal composition/lattice parameter, as schematized in Fig. 3b), a well-known phenomenon in substitutional solid solutions 32. The excellent agreement between DFT predictions and experimental data points displayed in Fig. 3.a suggests that chemical disorder is the unique source of microstrain in 'structurally-ordered' catalysts, thus confirming their defect-free nature (case (iii) in Fig. 2.b, observed for all PtNi catalysts but as a unique contribution solely for Cube, Sphere and Octahedron PtNi/C in Fig. 3.a). In contrast, since the dissolution of the less noble element of the alloy (commonly referred as 'dealloying') causes surface buckling and leads to the introduction of atomic vacancies in the topmost and near-surface layers 33 (case (iv) on Fig. 2.b), it is no surprise that higher microstrain values are found for 'structurally-disordered' catalysts (Hollow PtNi/C, Aerogel PtNi and Sponge PtNi/C). In fact, the 'structurally-disordered' catalysts are composed of dealloyed PtNi crystallites (*via* acid-treatment and/or long time exposure to corrosive medium, see the different materials synthesis protocols in Supplementary Information), interconnected to each other by grain boundaries, and so likely combine the three possible sources of microstrain (cases (ii)+(iii)+(iv) on Fig. 2.b).

At this stage of the paper, we note that microstrain is a global quantity 30. This makes the establishment of structure-activity relationships particularly arduous for heterogeneous electrocatalysis since (i) bulk defects contribute to increased microstrain values but are catalytically inactive and (ii) surface defects are catalytically active, but their contribution to microstrain depends on the crystallite size (*i.e.* is partially compensated by the bulk coherent domains). Here, by considering that the density of bulk defects (inhomogeneous alloying *e.g.* chemical disorder) is governed by the Ni content (as suggested by the DFT calculations displayed in Fig. 3.b), and that the compensation of surface defectiveness (grain boundaries, surface dealloying) by the bulk is determined by the surface-to-volume ratio, Eq. 1 was established:

$$\text{Microstrain} = f(\%\text{Ni}) + \text{Surface Distorsion} * D \quad \text{Eq.1}$$

Where the microstrain (in %% that is × 10.000) is the microstrain value derived from Rietveld refinement of the WAXS patterns, $f(\%\text{Ni})$ is the bulk contribution induced by inhomogeneous alloying directly linked to the average Ni content in the catalyst (Table S1), Surface Distortion (SD, in %) is a structural parameter that considers surface defectiveness, and D is the dispersion or 'Surface Atoms Ratio', as defined by Montejano-Carrizales *et al.* 34,35. Further details for the estimation of D, f and SD are provided by Eqs. S5-S16 and Fig. S4 in the Supplementary Information. As shown by Table S2 and Fig. S4, high values of microstrain do not necessarily translate into high SD values, the latter being controlled by the concentration of point (vacancies, adatoms) and surface defects (grain boundaries) but not by the Ni content.

The electrochemical properties of the different nanocatalysts were then investigated using the rotating disk electrode technique. Base cyclic voltammograms and ORR Tafel curves are presented in Fig. S5 and the values of specific ($SA_{0.95}$) and mass ($MA_{0.95}$) activity for the ORR, determined at $E = 0.95$ V *vs.* the reversible hydrogen electrode (RHE) after correction of oxygen diffusion in solution and of the Ohmic drop, are listed in Table S3. Fig. 4.a

displays the variations of $SA_{0.95}$ as a function of the SD descriptor. Two different branches are observed: the left branch is composed of monocrystalline catalysts featuring high ORR activity with small or null SD values. Low SD values actually translate the presence of homogeneously strained and densely packed surface, the ideal catalyst in this respect being the $Pt_3Ni(111)$-skin surface owing to its low affinity for oxygenated species 6. In this family of catalysts, an impressive current density of 567 ± 118 μ A cm_{Pt}^{-2} was determined at E = 0.95 V *vs.* RHE for Octahedron PtNi/C, reaching a 21-fold enhancement of the specific activity relative to the reference Pt/C TKK. On the other branch (Fig. 4.a), the specific activity for the ORR increases in a less pronounced manner with the values of SD.

Here, it is important to emphasize that, despite high ORR rates are obtained on both 'structurally-ordered' and 'structurally-disordered' catalysts, their operating mode is totally different from one to the other. As demonstrated by DFT calculations (see Fig. S6) and schematized in Fig. 4.b, in the 'structurally-ordered' family, the surface structure, chemical composition and elemental distribution are initially tailored to obtain a high density of catalytic sites with nearly optimal binding energy to the ORR intermediates (*i.e.* all the catalytic sites uniformly target the top of the Sabatier plot between ORR activity and the oxygen binding energy 7, see '$Pt_3Ni(111)$' surface in Fig. 4.b). In contrast, 'structurally-disordered' catalysts feature a wide distribution of catalytic site configurations, and those with the closest-to-optimal binding to the ORR intermediates most likely dominate the global reaction rate (see 'PtNi-defective' surface in Fig. 4.b). Using this scattergun approach toward improved ORR kinetics, a record mass activity was recently reported for the 'jagged' ultrafine Pt nanowires 27. Another remarkable aspect is that the multiplicity of catalytic site configurations present on their surface confers to 'structurally-disordered' catalysts enhanced kinetics for both reduction and oxidation reactions (note that these reactions do not necessarily occur on the same catalytic sites) 33. Thus, the presented SD descriptor provides fundamental insights into the catalytic mechanism at stake for a given bimetallic electrocatalyst.

We then confronted the ORR activity-surface distortion relationship presented in Fig. 4.a to the harsh operating conditions of a PEMFC cathode. To simulate the combined effects of acidic pH, oxidizing atmosphere and electrode potential, the spherical, cubic and octahedral PtNi/C samples were acid-treated in 1 M H_2SO_4 for 22 h at room temperature under air atmosphere (open circuit potential close to 1.0 V *vs.* RHE). The acid-treated samples are referred to as Sphere PtNi/C-AT, Cube PtNi/C-AT and Octahedron PtNi/C-AT below. Note that, because they were already dealloyed (see Supplementary Information), this procedure was not applied to the 'structurally-disordered' materials. Besides, the best-performing ORR nanocatalysts in their respective class of materials (Octahedron PtNi/C and Sponge PtNi/C) were selected, and aged using a 'load cycle' protocol consisting in 20,000 potential cycles at 50 mV s^{-1} between 0.6 and 1.0 V *vs.* RHE in Ar-saturated 0.1 M $HClO_4$ at T = 80 °C. To gain insights into the structural and chemical changes, WAXS and STEM/X-EDS characterizations and electrochemical measurements were performed before and after 100, 5,000 and 20,000 potential cycles on independent electrodes (Tables S4 to S6). A 'zero' cycle experiment (referred to as 'after 2^{nd} ORR'), consisting of the application of two consecutive electrochemical measurement protocols, was also performed to quantify the

impact of initial electrochemical conditioning and characterization on the catalysts' activity for the ORR.

It is clear from Fig. 5 that the surface distortion descriptor is robust enough to capture the catalysts changes in structure and chemistry under various (electro)chemical environments. Higher values of SD are observed for the 'structurally-ordered' nanocatalysts upon acidic treatment and/or potential cycling, suggesting surface reconstruction due to dissolution of Ni atoms from the topmost and the near-surface layers and/or nanoparticle aggregation (see STEM/X-EDS elemental profiles in Figs. S7 and S8 and TEM images in Figs. S9 and S10). Due to the combination of these morphological and chemical factors, the initially ordered catalysts exit the 'structurally-ordered' branch of the plot and a sharp decrease of the ORR specific activity is observed. This is particularly noticeable in the case of the Sphere PtNi/C sample for which the massive dissolution of the Ni-rich regions of the raw material in acidic solution led to the formation of porous nanoparticles (Fig. S9.b), in agreement with former literature reports 36–38. Strikingly, the value of SD on this catalyst changed from almost zero (raw material) to a value close to that of the porous Hollow PtNi/C catalyst (Figs. 4.a and 5.b). This degradation-induced transition from an approach (maintaining structural order) to the other (introducing structural disorder) led to a *ca.* 70 % retention of the initial ORR activity, while only 40-50 % of the initial ORR activity was retained after acidic treatment for Cube and Octahedron PtNi/C. Conversely, for the 'structurally-disordered' catalysts, potential cycling led to decreased SD values and milder ORR activity changes (see also Tables S5-S6). These changes are associated to a decrease of the grain boundary content due to crystallite coalescence, and agree with former reports 26,39,40.

Fig. 6 eventually demonstrates the practical relevance of the SD descriptor towards improved ORR electrocatalysts. First, it is noteworthy that the gap in initial ORR specific activity between the Sponge PtNi/C and the Octahedron PtNi/C closed after only two consecutive ORR measurements (Fig. 6.b), suggesting that the structurally-disordered approach (initial high SD value) provides better stability under simulated PEMFC cathode conditions. This is confirmed by the 62 % and 34 % loss of ORR specific activity after 20,000 potential cycles for Octahedron PtNi/C and Sponge PtNi/C, respectively. Second, as the porosity was maintained during potential cycling (Fig. 5.a), high SD values translate into superior mass activity retention (see changes in mass activity for Sponge PtNi/C *vs.* Octahedron PtNi/C in Fig. 5.c). Third, as unambiguously shown in Fig. 6.d, the loss of the non-noble element (see also Table S4 and Fig. S11) and the associated relaxation of the Pt lattice parameter (usually pivotal for the activity of bimetallic electrocatalysts 41) were not detrimental to Sponge PtNi/C, which owes its ORR activity to the structurally-induced *local strain* instead of the chemically-induced *global strain*. This is a clear advantage for structurally-disordered catalysts (high SD values) considering the detrimental effects of dissolved metallic cation contamination on PEMFCs performance 42. In contrast, the lattice parameter remained strained for Octahedron PtNi/C even if Ni atoms were progressively leached out during the potential cycling test. As previously reported for 8-10 nm PtNi dealloyed crystallites 38,43,44, the Pt-rich shell lattice contraction is ensured by the high residual Ni content in the particle core (observed here by STEM/X-EDS linear scans, see Fig. S8.a). Nonetheless, this constant lattice contraction did not result in a sustained ORR activity enhancement, as the contributions of the ligand and ensemble effects vanished with the near-surface Ni

composition and the disappearance of the octahedral shape, respectively (Figs. 5.f and S10). Finally, only the evolution of the SD descriptor presented in Fig. 5.e can attest for the gain in ORR activity measured after 5,000 potential cycles in the case of the Octahedron PtNi/C catalyst: indeed, the latter could neither have been accounted for by the Ni content nor by the lattice parameter, since both remained unchanged during this period (Table S4 and Fig. S11). This suggests that, whatever the initial surface state of the electrocatalysts, the surface distortion controls the ORR activity in the long-term. Thus, if the 'structurally-ordered' catalyst design approach leads to the best initial electrocatalytic performances, in light of the SD descriptor, the 'structurally-disordered' one appears more promising towards a sustainable ORR mass activity enhancement under real PEMFC cathode conditions.

In summary, by combining synchrotron WAXS, STEM/X-EDS, DFT calculations and electrochemical measurements, the Surface Distortion was put forward as a new powerful structural descriptor that is able to capture the degree of surface defectiveness of any given bimetallic nanocatalyst. This structural descriptor was successfully used to rationalize the fundamental differences in ORR activity and mechanism of 'structurally-ordered' and 'structurally-disordered' PtNi catalysts during simulated PEMFC cathode conditions. Our results show for the first time that promoting initial surface defectiveness in bimetallic electrocatalysts results in a more sustainable ORR activity enhancement compared to surface science-inspired approach, as surface buckling ineluctably occurs under simulated PEMFC cathode operation. They also provide clear-cut evidence that the Surface Distortion descriptor can be practically used in the design of a new generation of more robust 'defective' electrocatalysts, thus providing a convenient tool to enable their application in real PEMFC devices.

Methods

Synthesis

Nine different protocols were used to synthesize the catalysts library evaluated in this study. For a complete description of the protocols, the reader is referred to the Supplementary Information section and the following references: Sphere PtNi 36, Cube PtNi/C 45, Cube Pt/C 45, Octahedron PtNi/C 45, Hollow PtNi/C 46, Aerogel PtNi 47 and Sponge PtNi/C 28.

Electron Microscopy (STEM/X-EDS and HAADF-HRSTEM)

The STEM/X-EDS elemental maps were acquired using a JEOL 2100F microscope operated at 200 kV equipped with a retractable large angle Silicon Drift Detector (SDD) Centurio detector. The X-EDS spectra were recorded on different magnifications, from hundreds to individual nanoparticles by scanning the beam in a square region of various sizes. The quantitative analyses were performed on Pt *L* and Ni *K* lines using the *K*-factors provided by the JEOL software. The HRSTEM images were acquired using a FEI–Titan Ultimate microscope. This microscope was equipped with two aberration correctors allowing a < 0.1 nm spatial resolution in STEM mode. If needed (better chemical contrast), images were collected on a High Angle Annular Dark Field detector.

Synchrotron WAXS Measurements

The synchrotron WAXS measurements were performed at ID31 beamline of the European Synchrotron Radiation facility (ESRF) in Grenoble, France. The high energy X-ray radiation (61 keV or 0.20 Å) was focused on the catalyst powders contained in a 1 mm diameter Kapton® capillary, and the scattered signal was collected using a Dectris Pilatus CdTe 2M detector positioned 300 mm behind the sample. The size of the beam at the sample position was 4 × 30 μm (vertical × horizontal). The energy, detector distance and tilts were calibrated using a standard CeO_2 powder and the 2D diffraction patterns were reduced to the presented 1D curves using pyFAI software package 48. For electrochemically aged samples, the aged catalyst thin films were collected from the glassy carbon electrode using a Kapton® tape and characterized in transmission mode.

Rietveld Refinements

Rietveld refinement of the WAXS patterns was performed to extract the crystallite size, lattice parameter and microstrain 49 using the *Fm3m* structure of Pt metal and the Fullprof software. The instrumental resolution function was determined by the refinement of the WAXS pattern of a CeO_2 standard powder. After several trials, the Thomson-Cox-Hastings profile function was adopted with possibility for uniaxial anisotropic broadening from size origin 50. The background of patterns was described by an interpolated set of points with refinable intensities (this procedure allowed a more accurate description of the background leading to improved diffraction peak profiles).

Density Functional Theory Calculations

A series of simulation cells were prepared by substituting at random the Pt atoms by Ni atoms in a perfect fcc cell made of 500 Pt atoms until the desired content in Ni was reached. Six simulation cells were built, involving 10, 20, 30, 40, 50 and 60 Ni at. %. The DFT calculations were performed using the Vienna *ab initio* simulation package (VASP) code within the projector augmented wave (PAW) method. The general gradient approximation within the Perdew–Burke–Ernzerhof formulation was found an adequate choice for the exchange and correlation functional. The Hellmann–Feynman theorem was used to optimize the total volume of the cell and to relax the atomic positions after elemental substitution. We have considered that the atomic coordinates were fully relaxed when the amplitude of the individual forces were less than 0.001 eV $Å^{-1}$. Numerical integrations in the Brillouin zone were performed by means of the Hermite–Gaussian method. A single *k*-point (Γ point) was found adequate for total energies of the 500-atom cells to be converged within 10^{-4} eV with an energy cut-off of 260 eV. Supplementary 7-layer slabs were also built to illustrate the heterogeneity of catalytic sites in structurally-disordered nanomaterials. Briefly, to reproduce the ageing of bimetallic electrocatalysts in the PEMFC cathode environment, 35% atomic vacancies were introduced at random in a first pure Pt(111) slab but with a higher concentration in the surface layers. A second slab was built by substituting randomly 24 Pt atoms by Ni atoms in the three central layers of the previous slab, leading to a global Ni content of 12 at. % in the core of the slab. As the density of vacancies was identical in both cells, our approach allowed a quantitative estimation of the eventual influence of the presence of Ni atoms in the core layers on the chemisorption properties of the surface atoms

in structurally-disordered materials. More details and References are available in Supplementary Information.

Electrochemical measurements

All the glassware accessories used in this study were first cleaned by soaking in a H_2SO_4:H_2O_2 mixture for at least 12 hours, thoroughly washing and then boiling in Milli-Q water (Millipore, 18.2 MΩ cm, total organic compounds < 3 ppb). An Autolab PGSTAT302N potentiostat and a custom-made four-electrode electrochemical cell thermostated at T = 25 °C were used. The electrolyte (0.1 M $HClO_4$) was daily prepared using Milli-Q water and $HClO_4$ 96 wt. % (Suprapur®, Merck). The counter-electrode was a Pt grid and the reference electrode a commercial RHE (Hydroflex, Gaskatel GmbH) connected to the cell via a Luggin capillary. A Pt wire connected to the reference electrode was used to filter high frequency electrical noise. To prepare the working electrodes, a suspension containing 10 mg of the targeted ~20 wt. % Pt(Ni) catalyst powder, 54 μL of 5 wt. % Nafion® solution (Electrochem. Inc.), 1446 μL of isopropanol and 3.6 mL (18.2 MΩ cm) of deionized water (MQ-grade, Millipore) was made. After sonication for 15 minutes, 10 μL of the suspension was pipetted onto a 0.196 cm^2 glassy carbon disk under rotation at 700 rpm, and gently dried with a heat gun while the rotation was maintained to ensure evaporation of the Nafion® solvents, yielding a loading of *ca.* 20 μg_{Pt} cm^{-2}_{geo}. Prior to any electrochemical experiment, the working electrode was immersed into the deaerated electrolyte at E = 0.40 V *vs.* RHE (Ar >99.999 %, Messer). The following electrochemical techniques were then sequentially performed:

Step 1: Impedance Electrochemical Spectroscopy (EIS) measurements (E = 0.4 V *vs.* RHE, ΔE = 10 mV, 20 frequencies between 20 Hz and 100 kHz) were performed to determine the Ohmic resistance of the cell. 90% of the resistance value was then dynamically compensated by the potentiostat software (Nova 2.1).

Step 2: the base cyclic voltammograms were recorded in Ar-saturated electrolyte between 0.05 V and 1.23 V *vs.* RHE with a potential sweep rate of 500 (50 potential cycles, activation step) or 20 mV s^{-1} (3 potential cycles, base voltammograms).

Step 3: the Pt electrochemically active surface area (ECSA) was estimated using CO_{ads} stripping coulometry. In brief, a monolayer of CO_{ads} was formed on the electrocatalyst surface by bubbling CO gas (> 99.997 %, Messer) in the electrolyte for 6 min while keeping the electrode potential at E = 0.1 V *vs.* RHE, purging with Ar for 34 min while remaining at the same potential, and finally stripping off (oxidizing) this CO_{ads} layer by recording 3 cyclic voltammograms between 0.05 V and 1.23 V *vs.* RHE at 20 mV s^{-1}. The electrical charge required to electrooxidize the CO_{ads} monolayer provided the ECSA assuming a conversion factor of 420 μC per cm^2 of Pt.

Step 4: the electrocatalytic activity for the ORR was measured in O_2-saturated 0.1 M $HClO_4$ solution (20 minutes of purging by oxygen > 99.99 %, Messer, while maintaining the electrode potential at E = 0.4 V *vs.* RHE) using cyclic voltammetry between 0.20 and 1.05 V *vs.* RHE at a potential sweep rate of 5 mV s^{-1} and at different rotational speeds in the order: 400 (2 times), 900, 1600, 2500 and 400 rpm again. The kinetic current for the ORR was

Europe PMC Funders Author Manuscripts

calculated on the 1600 rpm positive-going potential scan after correction of Ohmic drop and O_2 diffusion in solution (Koutecky-Levich equation, see Eq. S3).

The accelerated stress tests were performed in a second electrochemical cell containing fresh 0.1 M $HClO_4$ electrolyte and thermostated at T = 80 °C. The 'durability' cell was in all points similar to the 'characterization' cell except that, in order to avoid Pt dissolution at the counter electrode/Pt^{z+} ions redeposition at the working electrode, the Pt grid was replaced by a glassy carbon plate. The potential of the working electrode was cycled between 0.6 and 1.0 V *vs.* RHE using a linear potential ramp and a potential sweep rate of 50 mV s^{-1}. The various amounts of potential cycles (2^{nd} ORR, 100, 5,000 and 20,000) were performed on individual electrodes. Consequently, each electrode was electrochemically characterized twice (before and after cycling), only the number of potential cycles changed.

Supplementary Material

Refer to Web version on PubMed Central for supplementary material.

Acknowledgements

This work was performed within the framework of the Centre of Excellence of Multifunctional Architectured Materials 'CEMAM' n° ANR-10-LABX-44-01. The authors acknowledge financial support from the Grand Equipement National de Calcul Intensif (GENCI, grant number INP2227/72914), from the French National Research Agency (grant number ANR-14-CE05-0003-01), from the Swiss National Science Foundation (grant number 20001E_151122/1), from the German Research Foundation (DFG, grant number STR 596/5-1 and EY 16/18-1), from the German Federal Ministry of Education and Research (BMBF, grant number 03SF0527A), and from the European Research Council (grant number ERC AdG 2013 AEROCAT). The authors are grateful to Dr. Gwenn Cognard and Dr. Vincent Caldeira for their contribution to the manuscript's artwork.

References

1. Turner JA. Sustainable hydrogen production. Science. 2004; 305:972–4. [PubMed: 15310892]
2. Eberle DU, von Helmolt DR. Sustainable transportation based on electric vehicle concepts: a brief overview. Energy Environ Sci. 2010; 3:689.
3. Hansen J, et al. Dangerous human-made interference with climate: A GISS modelE study. Atmos Chem Phys. 2007; 7:2287–2312.
4. Steele BCH, Heinzel A. Materials for fuel-cell technologies. Nature. 2001; 414:345–352. [PubMed: 11713541]
5. Rabis A, Rodriguez P, Schmidt TJ. Electrocatalysis for polymer electrolyte fuel cells : Recent achievements and future challenges. ACS Catal. 2012; 2:864–890.
6. Stamenkovic VR, et al. Improved oxygen reduction activity on $Pt_3Ni(111)$ via increased surface site availability. Science. 2007; 315:493–497. [PubMed: 17218494]
7. Nørskov JK, et al. Origin of the overpotential for oxygen reduction at a fuel-cell cathode. J Phys Chem B. 2004; 108:17886–17892.
8. Stamenkovic V, et al. Changing the activity of electrocatalysts for oxygen reduction by tuning the surface electronic structure. Angew Chemie - Int Ed. 2006; 45:2897–2901.
9. Paffett MT, Daube KA, Gottesfeld S, Campbell CT. Electrochemical and surface science investigations of PtCr alloy electrodes. J Electroanal Chem. 1987; 220:269–285.
10. Bardi U, Beard BC, Ross PN. Surface oxidation of a $Pt_{80}Co_{20}$ alloy - An X-ray photoelectron spectroscopy and low energy electron diffraction study on the [100] and [111] oriented single crystal surfaces. J Vac Sci Technol A. 1988; 6:665–670.
11. Paffett MT, Beery JG, Gottesfeld S. Oxygen reduction at $Pt_{0.65}Cr_{0.35}$, $Pt_{0.2}Cr_{0.8}$ and roughened platinum. J Electrochem Soc. 1988; 135:1431–1436.

12. Hammer B, Nørskov JK. Electronic factors determining the reactivity of metal surfaces. Surf Sci. 1995; 343:211–220.
13. Gauthier Y, et al. Pt_xNi_{1-x}(111) alloy surfaces: structure and composition in relation to some catalytic properties. Surf Sci. 1985; 162:342–347.
14. Bligaard T, Nørskov JK. Ligand effects in heterogeneous catalysis and electrochemistry. Electrochim Acta. 2007; 52:5512–5516.
15. Hammer B, Nørskov JK. Theoretical surface science and catalysis — calculations and concepts. Adv Catal. 2000; 45:71–129.
16. Greeley J, Nørskov JK, Mavrikakis M. Electronic structure and catalysis on metal surfaces. Annu Rev Phys Chem. 2002; 53:319–348. [PubMed: 11972011]
17. Cui C, Gan L, Heggen M, Rudi S, Strasser P. Compositional segregation in shaped Pt alloy nanoparticles and their structural behaviour during electrocatalysis. Nat Mater. 2013; 12:765–771. [PubMed: 23770725]
18. Beermann V, et al. Rh-doped Pt-Ni octahedral nanoparticles: Understanding the correlation between elemental distribution, oxygen reduction reaction, and shape stability. Nano Lett. 2016; 16:1719–1725. [PubMed: 26854940]
19. Beermann V, et al. Tuning the electrocatalytic oxygen reduction reaction activity and stability of shape-controlled Pt-Ni nanoparticles by thermal annealing - Elucidating the surface atomic structural and compositional changes. J Am Chem Soc. 2017; 139:16536–16547. [PubMed: 29019692]
20. Van Der Niet MJTC, Garcia-Araez N, Hernández J, Feliu JM, Koper MTM. Water dissociation on well-defined platinum surfaces: The electrochemical perspective. Catal Today. 2013; 202:105–113.
21. Farias MJS, Camara GA, Feliu JM. Understanding the CO preoxidation and the intrinsic catalytic activity of step sites in stepped Pt surfaces in acidic medium. J Phys Chem C. 2015; 119:20272–20282.
22. Gómez-Marín AM, Feliu JM. Oxygen reduction on nanostructured platinum surfaces in acidic media: Promoting effect of surface steps and ideal response of Pt(111). Catal Today. 2015; 244:172–176.
23. Sugimura F, Nakamura M, Hoshi N. The oxygen reduction reaction on kinked stepped surfaces of Pt. Electrocatalysis. 2017; 8:46–50.
24. Calle-Vallejo F, et al. Finding optimal surface sites on heterogeneous catalysts by counting nearest neighbors Federico. Science. 2015; 350:185–190. [PubMed: 26450207]
25. Calle-Vallejo F, Pohl MD, Bandarenka AS. Quantitative coordination-activity relations for the design of enhanced Pt catalysts for CO electro-oxidation. ACS Catal. 2017; 7:4355–4359.
26. Dubau L, et al. Defects do catalysis : CO monolayer oxidation and oxygen reduction reaction on hollow PtNi/C nanoparticles. ACS Catal. 2016; 6:4673–4684.
27. Li M, et al. Ultrafine jagged platinum nanowires enable ultrahigh mass activity for the oxygen reduction reaction. Science. 2016; 354:1414–1419. [PubMed: 27856847]
28. Chattot R, et al. Beyond strain and ligand effects: Microstrain-induced enhancement of the oxygen reduction reaction kinetics on various PtNi/C nanostructures. ACS Catal. 2017; 7:398–408.
29. Calle-Vallejo F, et al. Why conclusions from platinum model surfaces do not necessarily lead to enhanced nanoparticle catalysts for the oxygen reduction reaction. Chem Sci. 2017; 8:2283–2289. [PubMed: 28451330]
30. Langford JI, Lou D. Powder diffraction. Rep Prog Phys. 1996; 59:131–234.
31. Stukowski A, Markmann J, Weissmüller J, Albe K. Atomistic origin of microstrain broadening in diffraction data of nanocrystalline solids. Acta Mater. 2009; 57:1648–1654.
32. Kurlov AS, Gusev AI. Determination of the particle sizes, microstrains, and degree of inhomogeneity in nanostructured materials from X-ray diffraction data. Glas Phys Chem. 2007; 33:276–282.
33. Le Bacq O, et al. Effect of atomic vacancies on the structure and the electrocatalytic activity of Pt-rich/C nanoparticles: A combined experimental and density functional theory study. ChemCatChem. 2017; 9:2324–2338.

34. Montejano-Carrizales JM, Aguilera-Granja F, Morán-López JL. Direct enumeration of the geometrical characteristics of clusters. Nanostructured Mater. 1997; 8:269–287.
35. Montejano-Carrizales JM, Morán-López JL. Geometrical characteristics of compact nanoclusters. Nanostructured Mater. 1992; 1:397–409.
36. Gan L, Rudi S, Cui C, Heggen M, Strasser P. Size-controlled synthesis of sub-10 nm $PtNi_3$ alloy nanoparticles and their unusual volcano-shaped size effect on ORR electrocatalysis. Small. 2016:3189–3196. [PubMed: 27152487]
37. Gan L, Cui C, Rudi S, Strasser P. Core-shell and nanoporous particle architectures and their effect on the activity and stability of Pt ORR electrocatalysts. Top Catal. 2014; 57:236–244.
38. Strasser P, et al. Lattice-strain control of the activity in dealloyed core–shell fuel cell catalysts. Nat Chem. 2010; 2:454–460. [PubMed: 20489713]
39. Grammatikopoulos P, Cassidy C, Singh V, Sowwan M. Coalescence-induced crystallisation wave in Pd nanoparticles. Sci Rep. 2014; 4:1–9.
40. Asset T, et al. Elucidating the mechanisms driving the aging of porous hollow PtNi/C nanoparticles by means of CO_{ads} stripping. ACS Appl Mater Interfaces. 2017; 9
41. Kitchin JR, Nørskov JK, Barteau MA, Chen JG. Role of strain and ligand effects in the modification of the electronic and chemical properties of bimetallic surfaces. Phys Rev Lett. 2004; 93:4–7.
42. Kienitz B, Pivovar B, Zawodzinski T, Garzon FH. Cationic contamination effects on polymer electrolyte membrane fuel cell performance. J Electrochem Soc. 2011; 158:B1175.
43. Gan L, Heggen M, Rudi S, Strasser P. Core−shell compositional fine structures of dealloyed Pt_xNi_{1-x} nanoparticles and their impact on oxygen reduction catalysis. Nano Lett. 2012; 12:5423–5430. [PubMed: 22978641]
44. Oezaslan M, Hasché F, Strasser P. Pt-based core–shell catalyst architectures for oxygen fuel cell electrodes. J Phys Chem Lett. 2013; 4:3273–3291.
45. Zhang J, Yang H, Fang J, Zou S. Synthesis and oxygen reduction activity of shape-controlled Pt_3Ni nanopolyhedra. Nano Lett. 2010; 10:638–644. [PubMed: 20078068]
46. Bae SJ, et al. Facile preparation of carbon-supported PtNi hollow nanoparticles with high electrochemical performance. J Mater Chem. 2012; 22:8820.
47. Henning S, et al. Pt-Ni aerogels as unsupported electrocatalysts for the oxygen reduction reaction. J Electrochem Soc. 2016; 163:F998–F1003.
48. Ashiotis G, et al. The fast azimuthal integration Python library: PyFAI. J Appl Crystallogr. 2015; 48:510–519. [PubMed: 25844080]
49. Rodríguez-Carvajal J. Recent advances in magnetic structure determination by neutron powder diffraction. Phys B Condens Matter. 1993; 192:55–69.
50. Thompson P, Cox DE, Hastings JB. Rietveld refinement of Debye-Scherrer synchrotron X-ray data from Al_2O_3 . J Appl Crystallogr. 1987; 20:79–83.

Europe PMC Funders Author Manuscripts

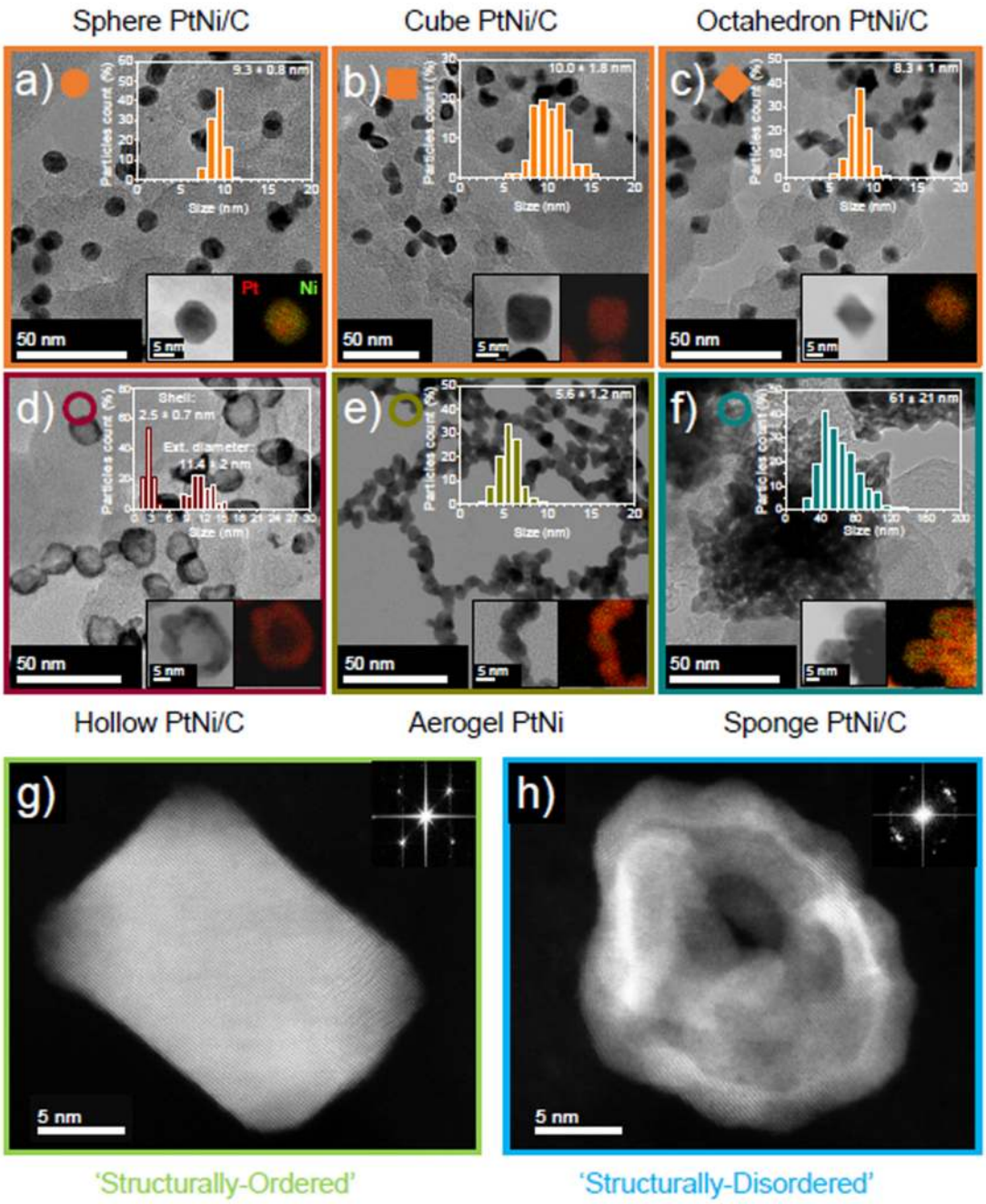

Figure 1. Morphological, structural and chemical characterizations of the various PtNi nanocatalysts synthesized in this study.

Transmission electron microscopy (TEM) image, associated particle size distribution (upper right insert) and scanning electron transmission microscopy coupled with X-ray energy dispersive spectroscopy (STEM/X-EDS) elemental map (lower right insert) of a) Sphere PtNi/C, b) Cube PtNi/C, c) Octahedron PtNi/C, d) Hollow PtNi/C, e) Aerogel PtNi and f) Sponge PtNi/C. High-angle annular dark-field-high resolution scanning transmission electron microscopy (HAADF-HRSTEM) image with insertion of its associated fast Fourier transform pattern of g) Cube Pt/C and h) Hollow PtNi/C. The HAADF-HRSTEM images

highlight the monocrystalline nature of the ‘structurally-ordered’ catalyst family (Sphere PtNi/C, Cube PtNi/C and Octahedron PtNi/C) whereas the ‘structurally-disordered’ family (Hollow PtNi/C, Aerogel PtNi and Sponge PtNi/C) features highly polycrystalline nanoparticles. For the Sponge PtNi/C catalyst, the particle size distribution in f) reflects the size of the overall aggregates.

Europe PMC Funders Author Manuscripts

Europe PMC Funders Author Manuscripts

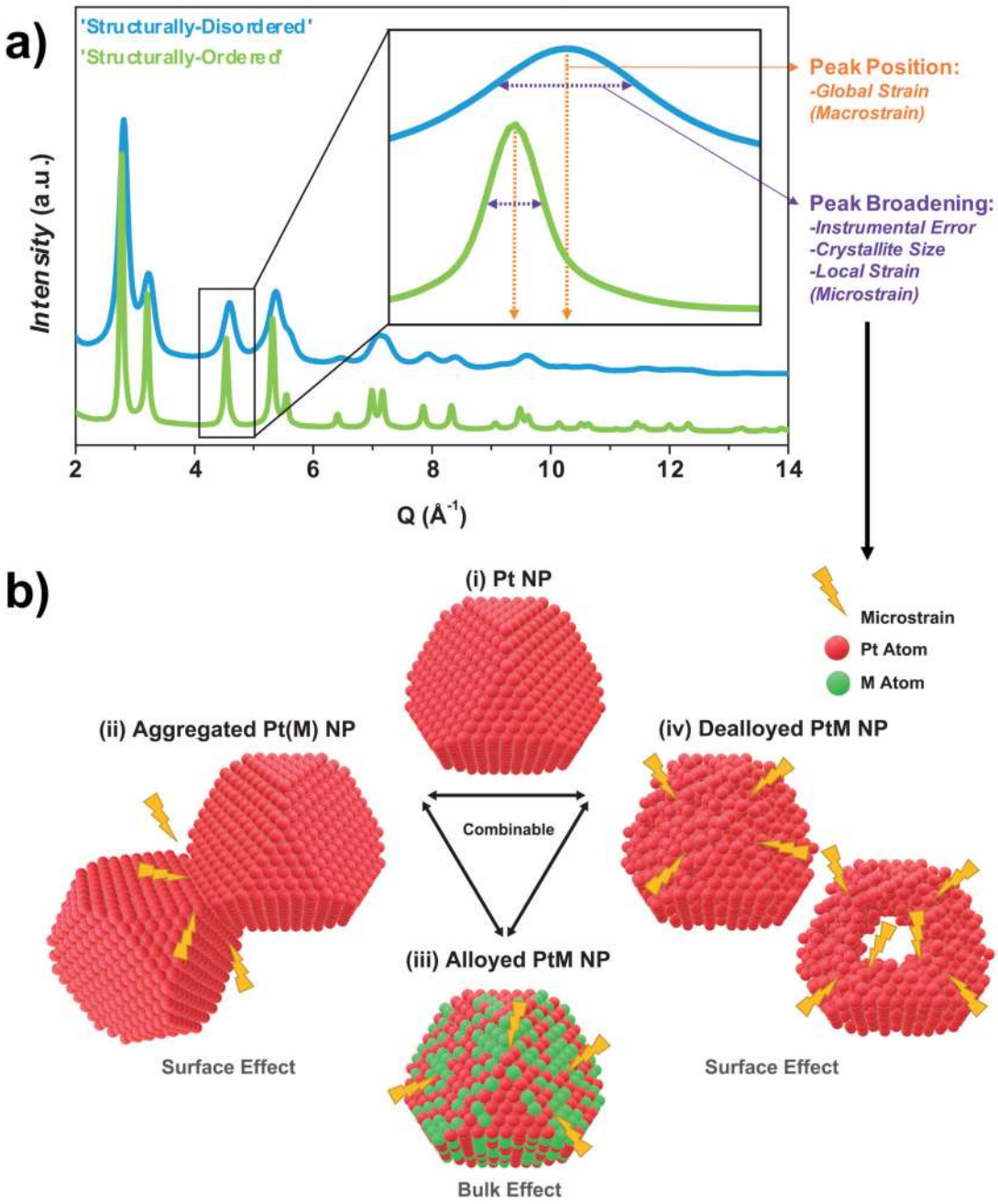

Figure 2. Experimental approach used to estimate the catalysts structural disorder through the extraction of microstrain from the synchrotron WAXS patterns.

a) Typical experimental WAXS patterns measured on structurally-disordered and structurally-ordered catalysts (here, Hollow PtNi/C and Cube Pt/C, respectively). The patterns are plotted as a function of the momentum transfer Q and b) possible sources of microstrain in bimetallic nanocatalysts (grain boundaries, inhomogeneous alloying or (electro)chemical surface destruction). The insert in a) shows the influence of macrostrain and microstrain on the position and the broadening of the WAXS reflections.

Europe PMC Funders Author Manuscripts

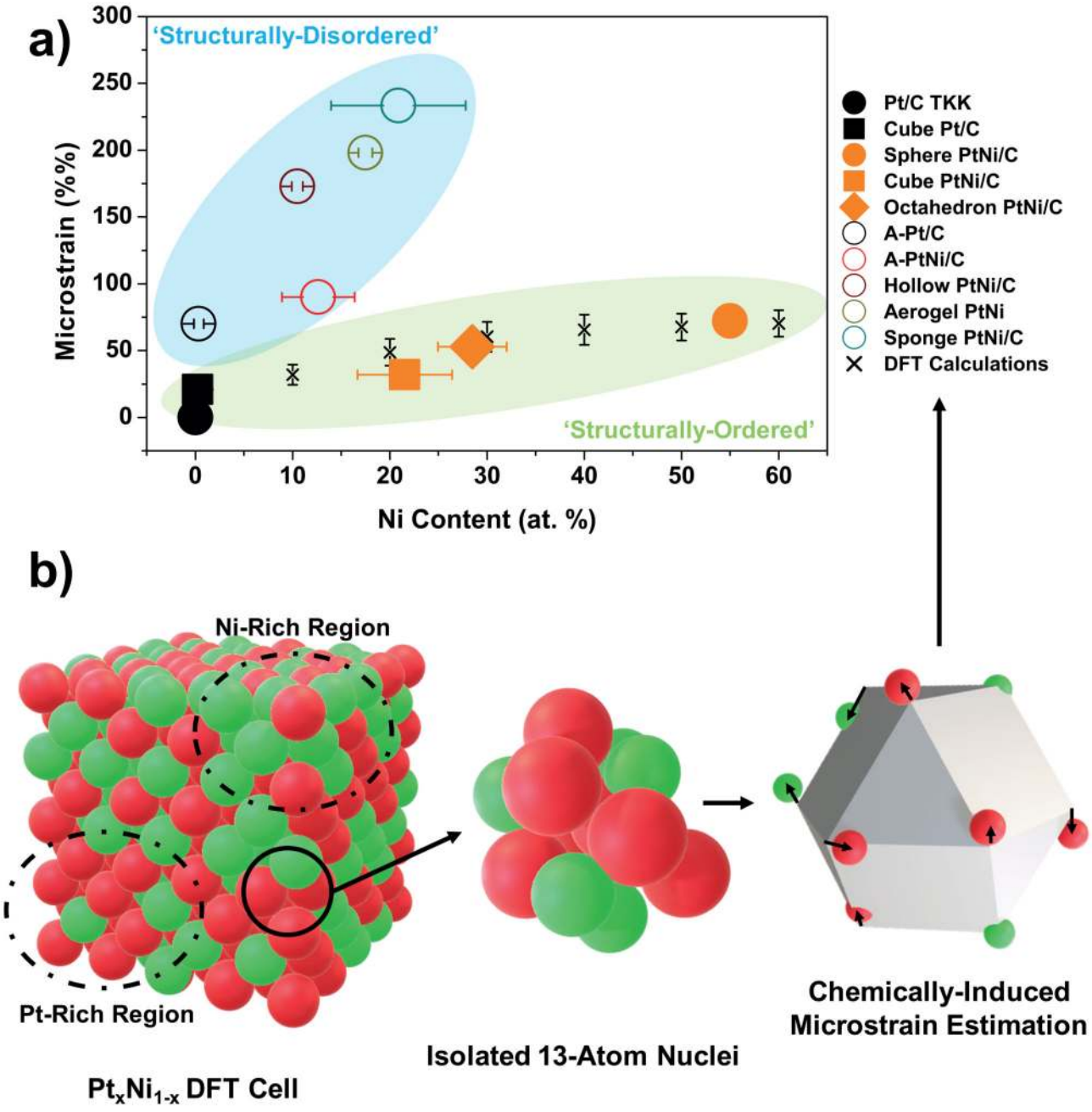

Figure 3. Disentangling the contribution of chemical disorder to the values of microstrain using DFT calculations.

a) Microstrain values obtained from Rietveld refinement of WAXS patterns plotted as a function of the averaged Ni content for all the electrocatalysts evaluated in this study and b) approach used in DFT calculations to estimate the contribution of chemical disorder to the values of microstrain. As summarized in b), the microstrain induced by the inhomogeneous distribution of Pt and Ni atoms in a 500-atom cell was estimated by calculating the deviation of an atom first neighbours shell shape from the theoretically perfect cuboctahedron usually encountered in a perfect bulk face-centred cubic (fcc) structure. More details are provided in

the Supplementary Information. The DFT calculations plotted in a) obtained by the approach presented in b) show that the microstrain measured in ‘structurally-ordered’ catalysts should be ascribed to chemical disorder. The x-axis error bars refer to standard deviation of the average Ni content estimated from STEM/X-EDS measurements on at least tens of nanoparticles (see Supplementary Table 1). The y-axis error bars were estimated by DFT calculations.

Europe PMC Funders Author Manuscripts

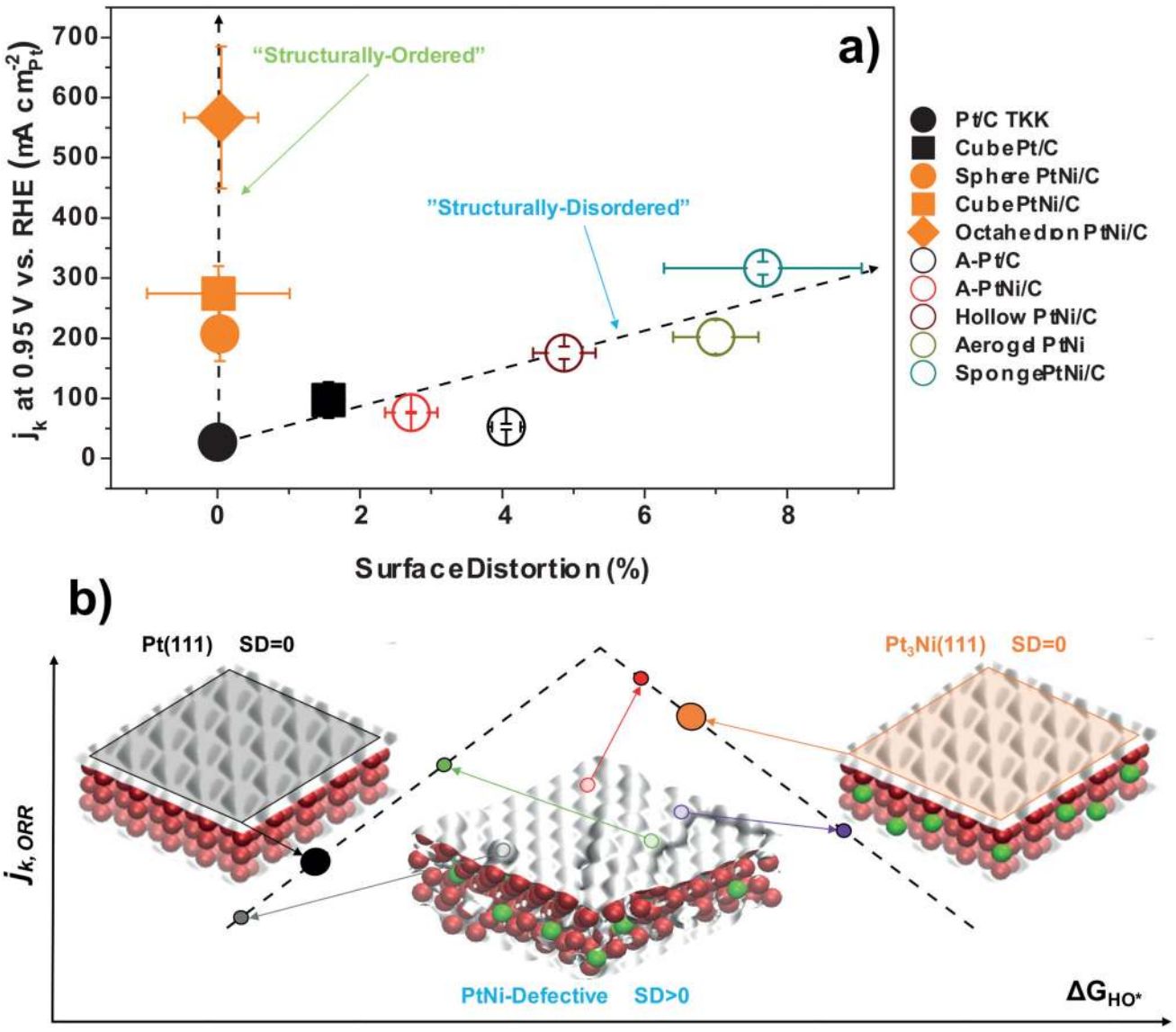

Figure 4. Relationships between the kinetic current for the ORR and Surface Distortion for the fresh electrocatalysts evaluated in this study.

a) experimental trends, b) DFT-derived schematic describing different approaches towards enhanced ORR kinetics: the scattergun approach (SD>0) vs. the homogeneously optimized surface approach (SD=0) for structurally-disordered and structurally-ordered catalysts, respectively. The ORR activity in a) was measured in O_2-saturated 0.1 M $HClO_4$ at a potential sweep rate of 5 mV s^{-1} and ω = 1600 rpm on at least three samples and the kinetic current (j_k) was extracted after correction of Ohmic losses and oxygen diffusion in solution (see Methods and Eq. S4 in the SI). The values of SD were calculated using the values of the microstrain and of the crystallite size estimated from Rietveld refinement of WAXS patterns and the Ni content estimated from WAXS and STEM/X-EDS analyses (see Supplementary equations (1) and (5)-(16)). The error bars represent the standard deviation of these quantities. The numerical values of the hydroxyl binding energy (ΔGHO*) relative to

Pt(111) schematized in b were calculated by means of DFT and can be found in Supplementary Fig. 6. The dotted lines in a) serve as guides to the eye.

Europe PMC Funders Author Manuscripts

Europe PMC Funders Author Manuscripts

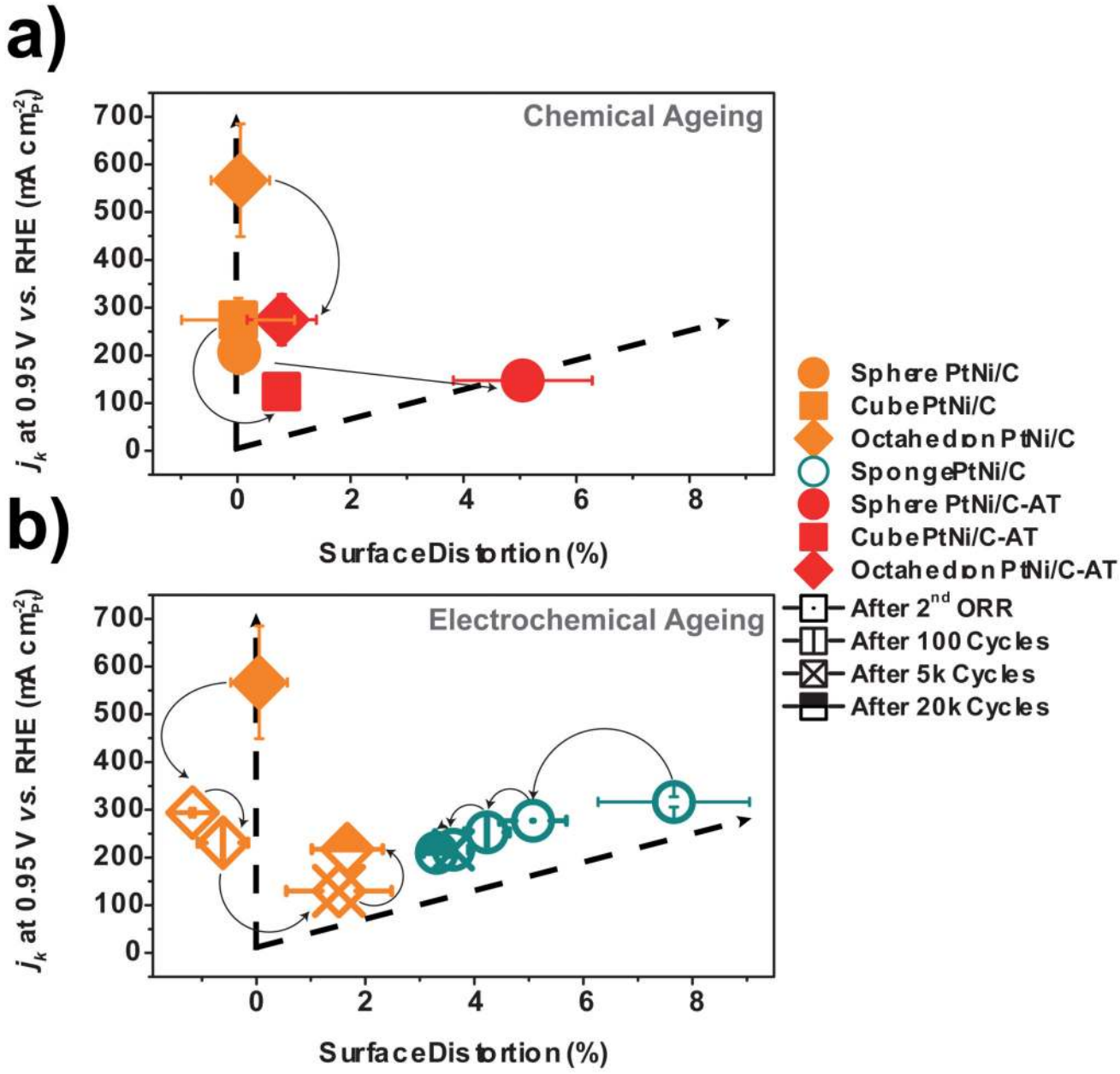

Figure 5. Evolution of the Surface Distortion-ORR activity plot after (electro)chemical ageing.

a) impact of acidic treatment (AT) in 1 M H_2SO_4 for 22 h on 'structurally-ordered' (Sphere, Cube and Octahedron PtNi/C) catalysts (referred as Sphere, Cube and Octahedron PtNi/C-AT), b) impact of electrochemical ageing (potential cycling in 0.1 M $HClO_4$ between 0.6 and 1.0 V vs. RHE at T = 80 °C) on Octahedron and Sponge PtNi/C. All dotted lines (similar from Fig. 4.a) serve as guides to the eye. The x- and y-axis error bars are the same as those defined in Fig. 4.

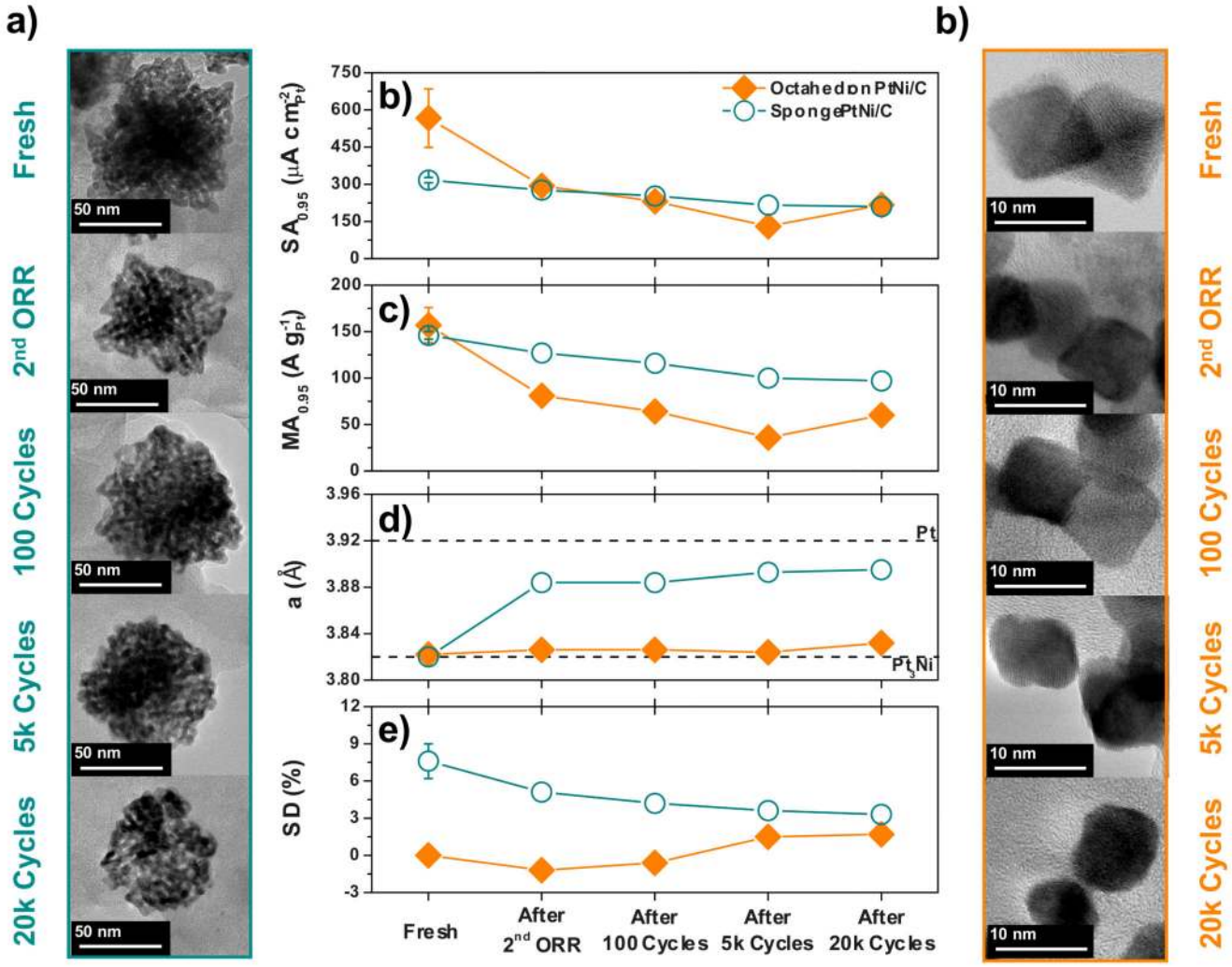

Figure 6. Structural and ORR activity changes under simulated PEMFC cathode environment.

a) STEM images of the Sponge, PtNi/C, b) specific activity c) mass activity, d) lattice parameter and e) SD descriptor of Sponge and Octahedron PtNi/C, and f) STEM images of the Octahedron PtNi/C after various potential cycling stages. The y-axis error bars are the same as those defined in Fig. 4.

Europe PMC Funders Author Manuscripts